Liu et al. *NPG Asia Materials* (2023) 15:9
https://doi.org/10.1038/s41427-022-00450-z

NPG Asia Materials

ARTICLE Open Access

Sodium preintercalation-induced oxygen-deficient hydrated potassium manganese oxide for high-energy flexible Mg-ion supercapacitors

Shude Liu[1,2], Ling Kang[3], Jian Zhang[3], Seong Chan Jun[1] and Yusuke Yamauchi[2,4]

Abstract

Layered potassium manganese oxides are promising candidates for use in aqueous supercapacitors owing to their wide potential windows, layered feature, and Faradaic redox reactions that occur on surfaces and in bulk regions. However, the practical application is hindered by rapid performance degradation due to their inherently low electrical conductivities and inferior structural stabilities. Here, we develop ultralong nanobelts comprising hydrated Na-intercalated oxygen-deficient potassium manganese oxide (H-Na-D-KMO), in which the Na^+ ions are preintercalated and synchronously induce the generation of oxygen vacancies, as high-energy-density and durable electrodes for Mg-ion supercapacitors. The experimental results indicated that preintercalation of Na^+ ions and formation of oxygen vacancies improved the electrical properties and ion diffusion, which accounted for the fast reaction kinetics and good cycling performance of H-Na-D-KMO. The optimized H-Na-D-KMO delivered a significantly enhanced specific capacitance and cycling performance compared to those of pure H-KMO. Asymmetric supercapacitors with H-Na-D-KMO as the cathode and as-prepared MoO_2@carbon as the anode exhibited an ultrahigh energy density of 108.4 Wh kg^{-1} at 11,000 Wh kg^{-1}, which is superior to most supercapacitors reported in the literature. Moreover, the assembled device exhibited good cycling stability for over 5000 cycles with a fading rate of 0.002% per cycle and good mechanical flexibility, which opens an avenue for further advancements in high-energy supercapacitors.

Introduction

With the rapidly increasing demand for portable and flexible electronic products, there is an urgent need for advanced energy storage techniques[1–3]. Among various energy storage systems, supercapacitors have emerged as promising candidates that bridge the gaps between batteries and traditional dielectric capacitors[4]. Although supercapacitors are superior in terms of rate capability, power density, and cycling lifespan, they still exhibit inferior energy densities[5,6]. This, in turn, significantly hinders practical application[7]. Specifically, the energy densities (E) of supercapacitors are determined by their specific capacitances (C) and working potential windows (V) via the relationship $E = 0.5\,C \cdot V^2$ [8]. Most transition metal-based materials store charges via surface Faradaic reactions[9,10], which undoubtedly limits the utilization of the electrode materials. Therefore, the development of efficient electrode materials with large potential windows and high bulk utilization at the atomic level is required to further improve energy density.

Recently, layered transition metal oxides have been shown to exhibit significant potential for use in supercapacitors owing to their efficient interlayer and accumulative surface/intercalation-based redox reactions[11]. They favor the migration of electrolyte ions and the achievement of large specific capacitance during cycling. In particular, potassium manganese oxides have attracted

Correspondence: Ling Kang (lkang@cee.ecnu.edu.cn) or Seong Chan Jun (scj@yonsei.ac.kr) or Yusuke Yamauchi (y.yamauchi@uq.edu.au)
[1]School of Mechanical Engineering, Yonsei University, Seoul 120-749, South Korea
[2]JST-ERATO Yamauchi Materials Space-Tectonics Project and International Center for Materials Nanoarchitectonics (WPI-MANA), National Institute for Materials Science, Tsukuba, Ibaraki 305-0044, Japan
Full list of author information is available at the end of the article

significant attention owing to their large theoretical charge storage capacities, wide potential windows, and highly abundant raw materials[12]. However, their electrochemical performance remains restricted mainly by intrinsically poor electronic conductivity, insufficient ion diffusion, and transport channels, and fast capacity fading upon cycling. To address these issues, the immense effort has been focused on developing carbonaceous material coating technologies and structural designs to improve electrical conductivity and suppress the dissolution of Mn^{2+} from Mn^{3+} disproportionation. Nevertheless, planar coatings often limit the diffusion capacities of electrolyte ions and block the exposed active sites of electrode materials; current structural architectures are not sophisticated enough to afford sufficient redox-active sites, which hinders full utilization of the active materials. Accordingly, improving the intrinsic electrical properties and structural stabilities of potassium manganese oxides while achieving fast ion diffusion kinetics remains a grand challenge.

Many aqueous electrochemical energy storage systems using multivalent metal ions (e.g., Mg^{2+}, Ca^{2+}, Zn^{2+}, and Al^{3+}) as charge carriers have shown great potential for large-scale energy storage[13,14]. This is because of their relatively high elemental abundances and large stable working potentials, which in principle, can provide high storage capacity[15,16]. Based on the aforementioned considerations, we developed a hydrated Na-intercalated oxygen-deficient potassium manganese oxide (H-Na-D-KMO) for Mg-ion supercapacitors. A series of experimental results showed that the introduction of Na^+ ions provided more paths to facilitate Mg^{2+} migration and induced more strain to create more active sites. This, in turn, improved the electrical conductivity and synergistically enhanced the electrochemical reactivity and cycling performance of H-Na-D-KMO. Consequently, the optimized H-Na-D-KMO exhibited a wide potential window while presenting an acceptable specific capacitance. When paired with the prepared MoO_2@carbon, the assembled H-Na-D-KMO//MoO_2@carbon asymmetric supercapacitors exhibited an unprecedented ultrahigh energy density of 108.4 Wh kg^{-1} at 1100 W kg^{-1} and good cycling stability with a capacitance fading rate of only 0.002% per cycle. Hence, this study will be of great interest for the rational design of electrode materials used in high-performance supercapacitors.

Results and discussion

The detailed synthetic process for H-Na-D-KMO with different concentrations of preintercalated Na^+ (denoted as H-Na-D-KMO-n ($n = 1$, 2, 3, and 4)) and its hydrated counterpart KMO (H-KMO) deposited on carbon cloth (CC) is described in the Experimental Section. Thermogravimetric analysis (TGA) was used to determine the interlayer water contents of the as-prepared samples. The TGA plots (Fig. S1) revealed two-step weight losses for H-KMO and H-Na-D-KMO-2, which were ascribed to the removal of adhered water (below 150 °C) and structural water (between 150 and 350 °C) within the materials[17]. The TGA results were used to determine the molecular formulas of H-KMO and H-Na-D-KMO-2, which were $KMO{\cdot}0.05H_2O$ and Na-D-$KMO{\cdot}0.07H_2O$, respectively. Inductively coupled plasma atomic emission spectrometry was performed to characterize the atomic ratios of Na and K. The relative atomic ratio of K in H-KMO was 1.88 at.%, and the relative atomic ratios of K and Na in H-Na-D-KMO-2 were 0.68 at.% and 2.05 at.%, respectively. Scanning electron microscopy (SEM) images showed that H-KMO exhibited a belt-like structure with lengths of several micrometers and lateral dimensions of 15–25 nm (Fig. S2), which were woven together and evenly deposited on the carbon cloth (CC) substrate. Energy-dispersive X-ray spectroscopy (EDS) maps revealed homogeneous distributions of the K, Mn, and O elements (Fig. S3). Conversely, H-Na-D-KMO-2 showed no obvious morphological changes (Fig. 1a, b). Transmission electron microscopy (TEM) was used to further characterize the nanobelt-like structure of H-Na-D-KMO-2 (Fig. 1c). A lattice fringe with a *d*-spacing of 0.698 nm was observed in the high-resolution TEM (HRTEM) image of H-KMO, which corresponded to the (001) plane (Fig. 1d). As shown in the HRTEM result for H-Na-D-KMO-2 (Fig. 1e), an interplanar spacing of 0.713 nm was identified for the (001) plane, which was slightly larger than that of H-KMO. This was potentially due to local distortions and stresses induced by Na^+ intercalation and O vacancies. This lattice spacing is large enough to accommodate sufficient Mg^{2+} (0.79 Å). Many dislocations and deformations (marked with dashed lines in Fig. 1e) were observed, which exposed additional active sites for high electrode reactivity. To experimentally explore the strain effects operating after preintercalation of Na^+, a geometric phase analysis (GPA) was conducted based on the HRTEM images. The GPA maps showed that the components along εxx obtained from the R2 region of H-Na-D-KMO-2 (Fig. 1g) exhibited more pronounced stress changes relative to the R1 region of H-KMO (Fig. 1f). Previous reports indicated that local strain introduced charge transfer and produced Jahn–Teller active Mn^{3+}, which kinetically facilitated electrochemical intercalation and desorption processes by lowering the critical migration barriers[18]. This internal strain accommodated mechanical strains due to volume expansion and avoided material pulverization. Moreover, the elemental maps of H-Na-D-KMO-2 indicated uniform distributions of O, Mn, K, and Na in the nanobelts (Fig. 1h).

The XRD pattern for H-KMO (Fig. 2a) shows four main characteristic peaks at 12.6°, 25.3°, 36.8°, and 65.0°, which are indexed to the (001), (002), (-111), and (020) planes of delta-type MnO_2 (JCPDS #43-1456), respectively,

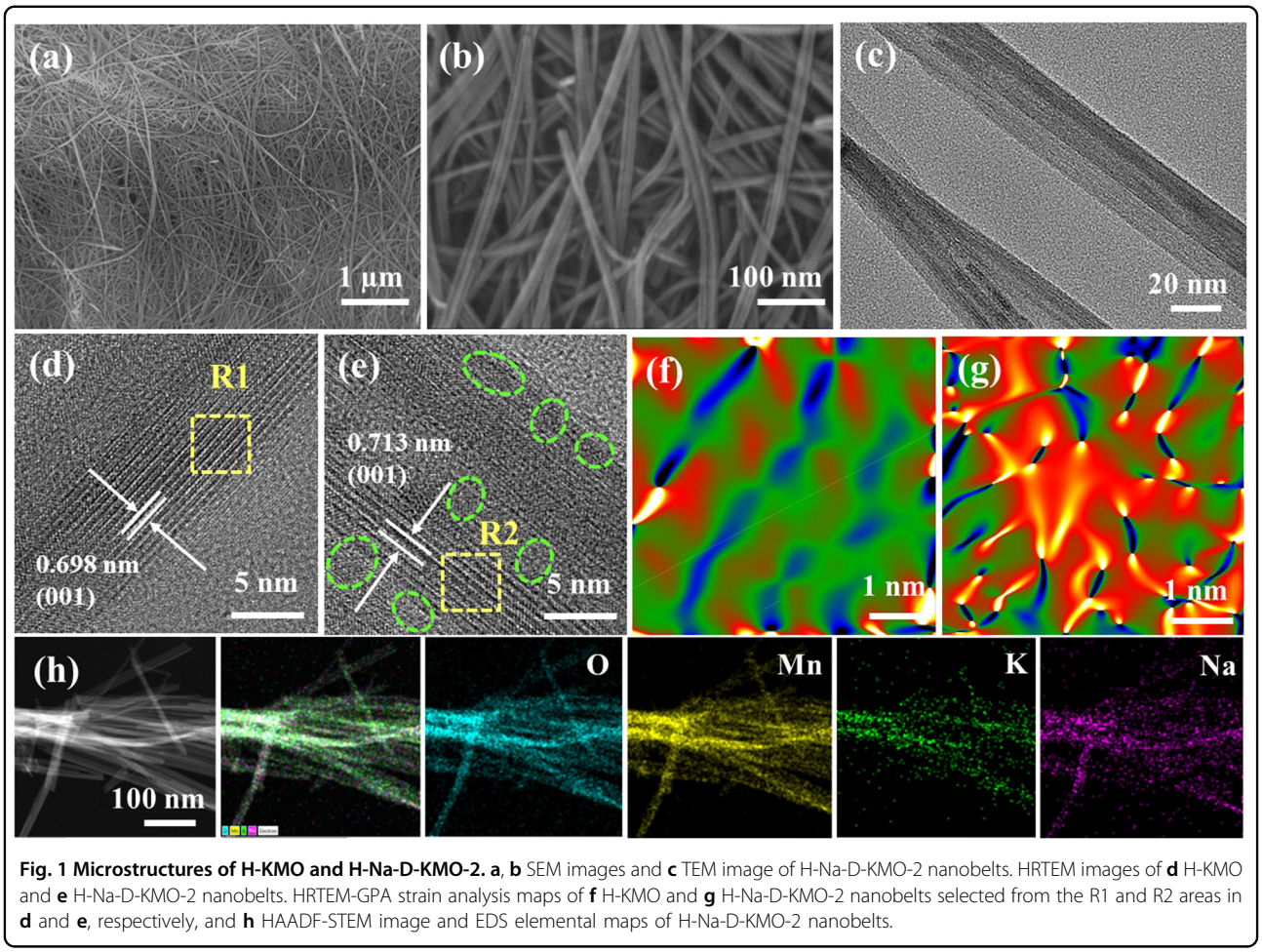

Fig. 1 Microstructures of H-KMO and H-Na-D-KMO-2. a, **b** SEM images and **c** TEM image of H-Na-D-KMO-2 nanobelts. HRTEM images of **d** H-KMO and **e** H-Na-D-KMO-2 nanobelts. HRTEM-GPA strain analysis maps of **f** H-KMO and **g** H-Na-D-KMO-2 nanobelts selected from the R1 and R2 areas in **d** and **e**, respectively, and **h** HAADF-STEM image and EDS elemental maps of H-Na-D-KMO-2 nanobelts.

consistent with a report on potassium manganese oxide[19]. As the level of Na^+ incorporation increased, the (001) diffraction peak gradually shifted to lower angles, indicating an expanded lattice spacing due to distortion after preintercalation. The Raman spectrum of H-KMO exhibited two major peaks at 649 and 576 cm^{-1} (Fig. 2b), which corresponded to the Mn-O stretching vibrations of the [MnO_6] octahedra and stretching vibrations in the basal plane of the [MnO_6] sheet, respectively[20], which confirmed the formation of a layered structure. With the increase in Na^+ preintercalation level, the peak intensity for H-Na-D-KMO gradually weakened compared with that of H-KMO, implying more defect formation within H-Na-D-KMO[21]. X-ray photoelectron spectroscopy (XPS) was performed to gain a deeper understanding of the elemental compositions of the as-prepared samples. Based on the K 2p XPS data for H-KMO and H-Na-D-KMO (Fig. S4a), the presence of K was confirmed. The Na 1 s spectrum of H-Na-D-KMO-2 showed a peak with a binding energy of 1070.6, which was assigned to Na^+ and revealed successful incorporation of Na^+ in H-Na-D-KMO-2[22]; however, there was no signal in the Na 1 s spectrum of H-KMO (Fig. S4b). The curve-fitted core level Mn 2p XPS data for H-KMO showed four deconvolved peaks, in which the two peaks at 654.2 and 642.5 eV matched well with known signals for Mn^{4+} and the other two peaks at 652.8 eV and 641.2 eV were indexed to Mn^{3+} [23]. For comparison, a negative shift was observed in the Mn 2p XPS peaks of H-Na-D-KMO-2; the ratio of Mn^{3+}/Mn^{4+} (calculated from the integrated areas in the fitted spectra) varied from 0.375 to 0.458 after Na^+ preintercalation, indicating decreased Mn valence in H-Na-D-KMO-2. The O 1 s XPS data (Fig. S5) for the prepared H-KMO presented three different binding energies for O1 (529.4 eV), O2 (531.0 eV), and O3 (531.9 eV), which corresponded to lattice oxygen, oxygen vacancies, and structural H_2O, respectively. The ratio of the oxygen vacancy peak for H-Na-D-KMO-2 was higher than that for H-KMO and revealed increased oxygen vacancies, and the atomic ratios of oxygen vacancies relative to oxygen contents were ~19.4% and 7.9%, respectively[24]. These results can be explained by a mechanism in which K + preintercalation induced the formation of low-valent Mn, which then promoted the generation of oxygen vacancies in H-Na-D-KMO to maintain the charge balance. Electron paramagnetic

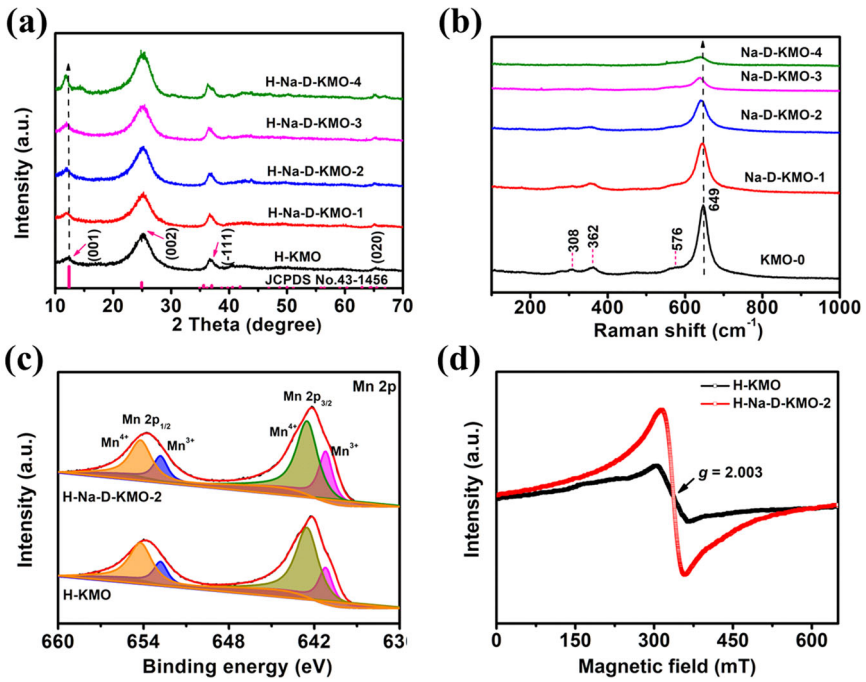

Fig. 2 Structural information of H-KMO and H-Na-D-KMO-n samples. a XRD patterns and **b** Raman spectra of H-KMO and H-Na-D-KMO-n (1, 2, 3, and 4). **c** High-resolution Mn 2p XPS spectra and **d** EPR curves for H-KMO and H-Na-D-KMO-2.

resonance (EPR) spectra (Fig. 2d) showed that H-Na-D-KMO-2 exhibited a signal at g = 2.003, which is the characteristic signal for e^- trapped in O vacancies[24]. Moreover, the signal density of the EPR curve for H-Na-D-KMO-2 was stronger than that for H-KMO, which indicated the presence of more abundant oxygen vacancies after preintercalation with Na^+This was consistent with the XPS results.

The electrochemical properties of the as-synthesized electrodes were evaluated by using a three-electrode configuration in 1 M $MgSO_4$ aqueous electrolyte. Cyclic voltammetry (CV) curves (Fig. 3a and Fig. S6) for H-KMO and H-Na-D-KMO-n (1, 2, 3, and 4) exhibited a wide, stable working potential window from −0.5 to 1.2 V (vs. AgCl/Ag), which was responsible for the high output energy and power densities of the corresponding full-cell devices[25]. Note that the charge contribution of the CC substrate to the entire electrode was negligible (Fig. S7). Figure 3b displays CV curves generated for the H-KMO and H-Na-D-KMO-n (1, 2, 3, and 4) electrodes in 1 M $MgSO_4$ aqueous electrolyte with a scan speed of 50 mV s^{-1}. Each CV curve exhibited a pair of broad redox peaks corresponding to reversible intercalation and deintercalation of Mg^{2+} into and from the layered structure. Moreover, H-Na-D-KMO-2 exhibited a larger enclosed CV area than other electrode materials, indicating the enhanced electrochemical reactivity of H-Na-D-KMO-2. This can be attributed to more ion transport paths and enhanced electrical conductivity of H-Na-D-KMO-2 due to the suitable incorporation of Na^+ ions and the induced oxygen vacancies, which improved the utilization of the active materials. It should be noted that the diffusion barrier was highly dependent on the lattice spacing; however, preintercalation of excess Na^+ ions can limit ion transport due to weakened bonding between Mg^{2+} and Mn or limit Mg^{2+} accommodation[26,27]. With increasing scan rates (Fig. 3a), the CV curves of H-Na-D-KMO-2 maintained symmetrical shapes without significant deformation over a wide range of scan rates. This indicated the high rate capability and low resistive behavior of H-Na-D-KMO-2.

The charge storage mechanism for the as-prepared samples was investigated with the relationship between scan rates (v) and current densities (I) observed for CV curves obtained at different scan rates (Fig. 3a and Fig. S6), and the power-law equation $I = a \cdot v^b$ was used. Specifically, the b-value corresponds to the slope of the log (v)–log (I) plot. Furthermore, $b = 0.5$ denotes a diffusion-controlled process, while $b = 1$ indicates a nondiffusion-controlled capacitive process. The b values for the cathodic peaks of H-KMO and H-Na-D-KMO-n (1, 2, 3, and 4) were estimated to be 0.65, 0.68, 0.72, 0.70, and 0.68, respectively (Fig. 3c), implying that the reaction current originated from a surface Faradaic redox reaction and ion intercalation. For comparison, H-Na-D-KMO-2 exhibited a higher b value than the other electrodes, indicating its

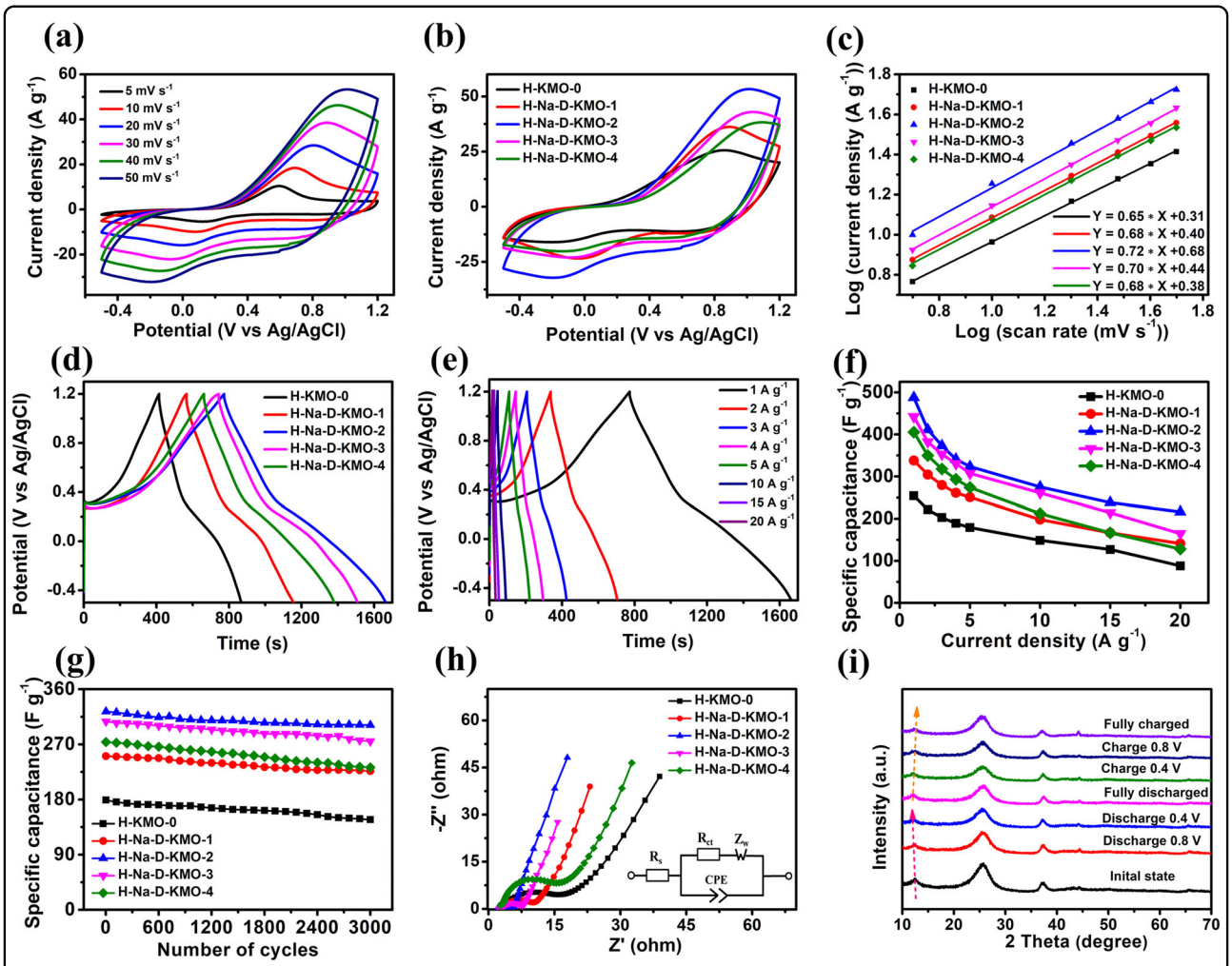

Fig. 3 Electrochemical properties of H-KMO and H-Na-D-KMO-n. a CV profiles of H-Na-D-KMO-2 at different scan rates. **b** Comparative CV profiles of H-KMO and H-Na-D-KMO-n (1, 2, 3, and 4). **c** Log(*i*) versus log(*v*) plots for H-KMO and H-Na-D-KMO-n (1, 2, 3, and 4). **d** Compared GCD profiles for H-KMO and H-Na-D-KMO-n (1, 2, 3, and 4). **e** GCD profiles of H-Na-D-KMO-2 at different current densities. Specific capacitances at different current densities (**f**), cycling stability tests at 10 A g^{-1} (**g**), and EIS plots (**h**) for H-KMO and H-Na-D-KMO-n (1, 2, 3, and 4). **i** XRD patterns of H-Na-D-KMO-2 at different charging/discharging states.

better reaction kinetics. This result indicated that ultra-long nanobelts significantly shortened the electrolyte ion transport paths and increased ion accessibility to the surface active sites, thereby favoring a surface capacitive-controlled contribution. Moreover, the synergistic effect of suitable preintercalation and induced oxygen vacancies in H-Na-D-KMO-2 further facilitated the rapid transfer of electrons and electrolyte ions.

As shown in Fig. 3d, e, and Fig. S8, the galvanostatic charge/discharge (GCD) curves of H-KMO and H-Na-D-KMO-n (1, 2, 3, and 4) exhibited nearly symmetric triangular shapes, consistent with the CV analysis. As expected, H-Na-D-KMO-2 exhibited a longer discharge time than the other electrodes (Fig. 3d), indicating the higher charge storage capacity of H-Na-D-KMO-2. This was due to proper Na^+ preintercalation, which provided sufficient charging paths and enhanced electrical conductivity to allow more efficient electrolyte permeation and enhance the ionic reaction kinetics. Additionally, the GCD curves of H-KMO and H-Na-D-KMO-n (1, 2, 3, and 4) recorded at different current densities exhibited almost symmetric shapes (Figs. 3e and S8), which revealed their high redox reversibility. The rate capability is a critical factor used to evaluate the practical application of supercapacitors. At a current density of 1 A g^{-1}, the calculated specific capacities of the H-KMO and H-Na-D-KMO-n (1, 2, 3, and 4) electrodes were 254, 338, 487, 442, and 406 F g^{-1}, respectively (Fig. 3f). When the current density was increased to 20 A g^{-1}, H-Na-D-KMO-2 maintained 44.4% of its initial capacity (217 F g^{-1}). Conversely, H-KMO, H-Na-D-KMO-1, H-Na-D-KMO-3, and H-Na-D-KMO-4 only remained the capacity retention

by 34.7%, 41.8%, 37.2%, and 31.6%, respectively. The cyclabilities of the as-prepared electrodes were explored with continuous GCD measurements run at 10 A g^{-1} over 3000 cycles. As illustrated in Fig. 3g, the H-Na-D-KMO-2 electrode maintained 93.2% of its initial value after the cycling test, which was higher than the retention rates of the other electrodes. Moreover, the sample displayed Coulombic efficiencies of nearly 100% upon cycling (Fig. S9), indicating fast ion diffusion kinetics. These results showed that proper ion preintercalation effectively suppressed the Jahn–Teller effect, thereby suppressing Mn dissolution and stabilizing the phase-transition structure of H-Na-D-KMO during cycling. Moreover, mechanically stable adhesion between H-Na-D-KMO-2 and highly conductive current collectors and an advanced layered structure led to enhanced electron conduction and effective ion transport.

To determine the reason for the excellent stability of H-Na-D-KMO-2, an SEM analysis was conducted after the cycling test. As shown in Fig. S10, the nanobelt morphology of H-Na-D-KMO was maintained. For comparison, the morphological structure of H-KMO exhibited obvious structural degradation (Fig. S11). No new impurities were identified from the XRD data for H-KMO and H-Na-D-KMO after cycling, (Fig. S12), which indicated that there was no phase transition during cycling. Electrochemical impedance spectroscopy (EIS) measurements were performed to study the enhanced electrochemical properties of H-Na-D-KMO-2. The resulting Nyquist plots for all electrodes exhibited similar shapes, including semicircles at high frequencies and nearly straight lines in the low-frequency range (Fig. 3h). The intersection on the real axis (Z') in the high-frequency region represents the series resistance (R_s), which comprises the internal resistance of the electrode materials, electrolyte resistance, and contact resistance between the electrode and electrolyte. The diameter of the arc along the real axis denotes the charge-transfer resistance (R_{ct}), and the linear part parallel to the imaginary axis represents the capacitive resistance. The R_s values of the H-KMO and H-Na-D-KMO-n (1, 2, 3, and 4) electrodes were calculated as 2.9, 2.4, 2.1, 2.4, and 2.7 Ω, respectively, while the corresponding R_{ct} values were 14.6, 9.4, 3.6, 5.9, and 10.8 Ω (Fig. S13). These findings indicated that H-Na-D-KMO-2 exhibited enhanced electrical properties and charge-transfer kinetics. Additionally, the slope of the EIS plot for the H-Na-D-KMO-2 electrode observed at low frequencies was slightly higher than those of the other electrodes, indicating its superior capacitive characteristics. In the ex situ XRD patterns obtained for H-Na-D-KMO-2 at different charge/discharge states, the (001) peak shifted slightly to a lower angle after discharge due to intercalation of Mg^{2+} into the H-Na-D-KMO-2 host (Fig. 3i). Conversely, the (001) peak shifted toward higher angles in the charged states, indicating a reversible Faradaic redox process.

Furthermore, MoO_2@carbon core-shell nanorods were prepared via a seed-assisted hydrothermal process followed by hydrothermal carbonization (see details in the Supporting Information). The crystal structure of MoO_2@carbon was confirmed by the presence of a set of characteristic MoO_2 diffraction peaks in the XRD pattern (Fig. S14)[28]. However, the characteristic diffraction peaks for the coated carbon were not observed, which was attributed to its amorphous nature, as noted in a previous report[29]. The core-shell nanorod morphology was indicated by the SEM analysis (Fig. S15a–c). The SEM image and the corresponding EDS maps clearly showed the presence of Mo, O, and C (Fig. S15d–g). The electrochemical behavior of MoO_2@carbon was estimated by using a 1 M $MgSO_4$ aqueous electrolyte. The CV curves for MoO_2@carbon showed several small pairs of redox peaks (Fig. S16a), which were attributed to Faradaic redox reactions between MoO_2 and Mg^{2+}, consistent with previous reports[30]. The shapes of the CV plots remained almost unchanged at different scan rates, indicating good rate capability. The approximately triangular and symmetric GCD curves confirmed good electrochemical reversibility (Fig. S16b). MoO_2@carbon exhibited a specific capacitance of 463 F g^{-1} at 1 A g^{-1}, and it retained a high value of 246 F g^{-1} when the current density was increased 20-fold (Fig. S16c). Hence, it is clear that the electrode exhibited high cycling durability with only a 9.3% decrease in capacitance after 5000 cycles at a high current density of 20 A g^{-1} (Fig. S16d). This excellent electrochemical performance indicates its potential for use as an anode material for supercapacitors.

To further evaluate the potential of H-Na-D-KMO for use in supercapacitor applications, the electrochemical performance of an asymmetric supercapacitor (ASC) device assembled using H-Na-D-KMO-2 as the cathode, MoO_2@carbon as the anode, and a piece of filter paper as the separator was investigated with $MgSO_4$/PVA used as a gel electrolyte. Three-electrode tests showed that the H-Na-D-KMO-2 cathode and MoO_2@carbon anode operated at a scan rate of 30 mV s^{-1} over potential windows of −0.5–1.2 V vs. AgCl/Ag and −1–0 V vs. AgCl/Ag, respectively (Fig. S17a). This demonstrated that the ASC devices assembled with H-Na-D-KMO and MoO_2@-carbon can be extended to an operating voltage of 2.2 V. The mass ratio of the positive electrode to the negative electrode was fixed at close to 1:1.7 based on the charge balance theory of ($Q^+ = Q^-$)[31]. The CV profiles obtained at 30 mV s^{-1} and GCD profiles at 1 A g^{-1} over different voltage windows for the as-fabricated ASC exhibited no obvious evolution until the voltage reached 2.2 V (Fig. 4a, b); hence, in the following measurements, the ASC devices will be performed at this voltage. The ASC device

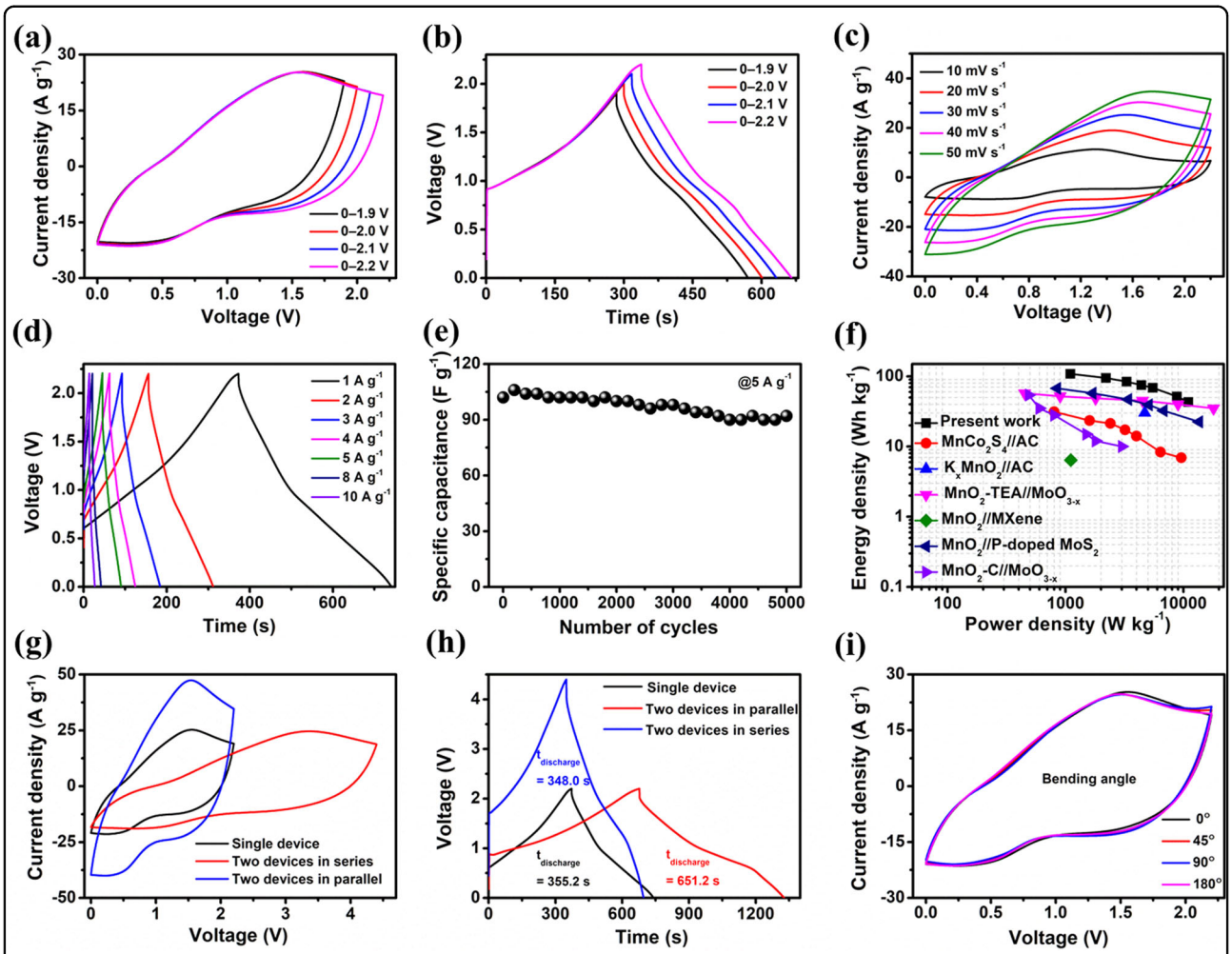

Fig. 4 Electrochemical properties of H-Na-D-KMO//MoO @carbon device. a CV profiles and **b** GCD profiles of the H-Na-D-KMO//MoO_2@carbon ASC device generated over different voltage windows at 30 mV s^{-1}. CV curves (**c**), GCD curves (**d**), cycling performance (**e**), and Ragone plots of our assembled device compared with ASC devices using Mn-based electrodes reported in the literature (**f**). **g** CV profiles of two as-assembled ASC devices connected in series and parallel at 30 mV s^{-1}. **h** GCD profiles of two as-assembled ASC devices connected in series and parallel at 1 A g^{-1}. **i** CV profiles obtained for the as-assembled ASC device held at different bending angles.

displayed nonrectangular CV curves at various scan rates, implying a mixed charge contribution from capacitive and diffusion-controlled processes (Fig. 4c). Furthermore, the shapes of the CV curves remained good when the scan rate was increased to 50 mV s^{-1}, indicating fast charge/discharge characteristics. GCD curves recorded in the current density range 1–10 A g^{-1} showed almost symmetric shapes, revealing high redox reversibility[32]. It is worth noting that the voltage plateaus observed in the GCD curves were consistent with the redox peaks in the CV curves (Fig. 4d) and indicated Faraday redox behavior. The rate capability curves of the ASC device exhibited a desirable specific capacitance of 161 F g^{-1} at 1 A g^{-1} while retaining 64 F g^{-1} at 10 A g^{-1} (Fig. S17b). The long-term cycling performance of the ASC device was evaluated at 5 A g^{-1} (Fig. 4e). The specific capacitance of the device increased during approximately the first 100 cycles due to the full activation of the active material. The device exhibited an impressive 90.2% capacity retention even after 5000 cycles, which was consistent with previously reported devices[33,34]. The device exhibited high Coulombic efficiencies above 97.4% over the whole cycling process (Fig. S18), indicating the high reversibility of the as-prepared electrode materials. The EIS plot of the ASC device indicated a small increase in R_{ct} after cycling (Fig. S17c), which potentially resulted from the blockage of some charge-transfer channels due to a slight structural collapse of the electrode material after long-term cycling. Figure 4f shows a Ragone plot depicting the relationship between energy and power density for flexible asymmetric batteries and the values reported for Mn-based electrode materials for comparison. The assembled asymmetric cells delivered an energy density of 108.4 Wh kg^{-1} at 1100 W kg^{-1} while retaining 43.1 W kg^{-1} at 11,000 Wh kg^{-1}, which is much

higher than those of previously reported ASC devices such as $MnCo_2S_4$//AC[35], K_xMnO_2//AC[36], MnO_2-triethanolamine (TEA)//MoO_{3-x}[37], MnO_2//MXene[38], MnO_2//P-doped MoS_2[39], and MnO_2-C//MoO_{3-x}[40]. Such high energies and power densities indicated that our assembled device holds great potential for practical applications.

The performance stability of an integrated assembly is critical for practical feasibility. Figure 4g and h shows the CV curves measured at 30 mV s^{-1} and GCD curves at 1 A g^{-1} for a single device and two devices connected in series and parallel, respectively. The voltage window for the two ASC devices connected in series was almost double that of the single device, while the two ASC devices connected in parallel exhibited almost double the discharging time, indicating high stability and reproducibility for the integrated ASC devices. As proof of practicality, a red light-emitting diode (LED; 2 V) was lit using the ASC device (Fig. S17d). Good flexibility is required for the development of portable and wearable electronic devices. To evaluate the flexibility of the assembled configuration, we measured the CV curves during bending at various angles. There was no obvious change in the capacitance during the bending tests (Fig. 4i), indicating excellent flexibility. As a demonstration, our assembled ASC device was easily wrapped around a finger and still maintained the power to a red LED with the light flashing on and off (Fig. S17e, f). Therefore, it is a promising energy storage system for use in portable devices.

Conclusions

In summary, we have developed Na^+ ion-intercalated and oxygen-deficient H-Na-D-KMO for Mg-ion supercapacitors. A comprehensive study suggested that the simultaneous incorporation of Na^+ and oxygen defects improved the electrical conductivity and facilitated ion diffusion to provide highly stable and active H-Na-D-KMO. Moreover, the ultralong nanobelts with 1D morphologies provide fast reaction kinetics for H-Na-D-KMO. The as-prepared H-Na-D-KMO, with its wide operating potential window, exhibited a desirable specific capacitance of 487 F g^{-1} at 1 A g^{-1} and good cycling stability. When paired with a MoO_2@carbon anode, the assembled H-Na-D-KMO//MoO_2@carbon quasi-solid-state ASC device realized a remarkable energy density of 108.4 Wh kg^{-1} at 1100 W kg^{-1}, which was superior to those of supercapacitor devices. The quasi-solid-state ASC devices exhibited good mechanical properties and no obvious capacitance delays with the different bending states. These findings enabled the energy storage capacity of our assembled device to approach battery levels while displaying both good mechanical flexibility and good cycling capability.

Acknowledgements
This work was supported by the Australian National Fabrication Facility's Queensland Node (ANFF-Q) and the JST-ERATO Yamauchi Materials Space-Tectonics Project (JPMJER2003). S.L. and S.C.J. gratefully acknowledge financial support from a National Research Foundation of Korea (NRF) grant funded by the Korean Government (MIST) (No. NRF-2019R1A2C2090443) and Technology Innovation Program('20013621', Center for Super Critical Material Industrial Technology) funded by the Ministry of Trade, Industry & Energy (MOTIE, Korea). This work was performed in part at the Queensland node of the Australian National Fabrication Facility, a company established under the National Collaborative Research Infrastructure Strategy to provide nano- and microfabrication facilities for Australian researchers.

Author details
[1]School of Mechanical Engineering, Yonsei University, Seoul 120-749, South Korea. [2]JST-ERATO Yamauchi Materials Space-Tectonics Project and International Center for Materials Nanoarchitectonics (WPI-MANA), National Institute for Materials Science, Tsukuba, Ibaraki 305-0044, Japan. [3]Shanghai Key Laboratory of Multidimensional Information Processing, East China Normal University, 500 Dongchuan Road, 200241 Shanghai, China. [4]Australian Institute for Bioengineering and Nanotechnology (AIBN), The University of Queensland, Brisbane, QLD 4072, Australia

Author contributions
S.L., K.K., S.C.J., and Y.Y. presented the conceptualization and designed the experiments. S.L., K.K., and J.Z. performed the experiments, wrote the original draft, and analyzed the data. S.C.J. and Y.Y. supervised the work. The paper was discussed by all authors.

Data availability
The authors declare that all the relevant data are available within the paper and its Supplementary Information file or from the corresponding author upon reasonable request.

Conflict of interest
The authors declare no competing interests.

Supplementary information The online version contains supplementary material available at https://doi.org/10.1038/s41427-022-00450-z.

Received: 31 August 2022 Revised: 4 November 2022 Accepted: 9 November 2022.
Published online: 24 February 2023

References

1. Gao, C. et al. A seamlessly integrated device of micro-supercapacitor and wireless charging with ultrahigh energy density and capacitance. *Nat. Commun.* **12**, 1–10 (2021).
2. Zhang, W. et al. Lignin derived porous carbons: synthesis methods and supercapacitor applications. *Small Methods* **5**, 2100896 (2021).
3. Zhang, W. et al. Accordion-like carbon with high nitrogen doping for fast and stable K ion storage. *Adv. Energy Mater.* **11**, 2101928 (2021).
4. Zhou, Y. et al. Ultrahigh-areal-capacitance flexible supercapacitor electrodes enabled by conformal P_3MT on horizontally aligned carbon-nanotube arrays. *Adv. Mater.* **31**, 1901916 (2019).
5. Li, K. et al. Tuning MnO_2 to FeOOH replicas with bio-template 3D morphology as electrodes for high performance asymmetric supercapacitors. *Chem. Eng. J.* **370**, 136–147 (2019).
6. Li, K. et al. Assembling a double shell on a diatomite skeleton ternary complex with conductive polypyrrole for the enhancement of supercapacitors. *Chem. Commun.* **55**, 13773–13776 (2019).
7. Sun, L. et al. Ionic liquid-based redox active electrolytes for supercapacitors. *Adv. Funct. Mater.* **32**, 2203611 (2022).

8. Kandambeth, S., Kale, V. S., Shekhah, O., Alshareef, H. N. & Eddaoudi, M. 2D covalent-organic framework electrodes for supercapacitors and rechargeable metal-ion batteries. *Adv. Energy Mater.* **12**, 2100177 (2022).
9. Zhang, W. et al. Lignin derived carbon materials: current status and future trends. *Carbon Res.* **1**, 1–39 (2022).
10. Li, K. et al. A multidimensional rational design of nickel–iron sulfide and carbon nanotubes on diatomite via synergistic modulation strategy for supercapacitors. *J. Colloid Interface Sci.* **603**, 799–809 (2021).
11. Kumar, K. S., Pandey, D. & Thomas, J. High voltage asymmetric supercapacitors developed by engineering electrode work functions. *ACS Energy Lett.* **6**, 3590–3599 (2021).
12. Liu, S. et al. Recent advances and perspectives of battery-type anode materials for potassium ion storage. *ACS Nano* **15**, 18931–18973 (2021).
13. Xie, J. & Zhang, Q. Recent Progress in multivalent metal (Mg, Zn, Ca, and Al) and metal-ion rechargeable batteries with organic materials as promising electrodes. *Small* **15**, 1805061 (2019).
14. Liang, Y., Dong, H., Aurbach, D. & Yao, Y. Current status and future directions of multivalent metal-ion batteries. *Nat. Energy* **5**, 646–656 (2020).
15. Shao, Y. et al. 3D crumpled ultrathin 1T MoS_2 for inkjet printing of Mg-ion asymmetric micro-supercapacitors. *ACS Nano* **14**, 7308–7318 (2020).
16. Liu, Z. et al. Ion migration and defect effect of electrode materials in multivalent-ion batteries. *Prog. Mater. Sci.* **125**, 100911 (2021).
17. Zhang, X. et al. Hydration enables air-stable and high-performance layered cathode materials for both organic and aqueous potassium-ion batteries. *Adv. Funct. Mater.* **32**, 2204318 (2022).
18. Peng, H. et al. The coupling of local strain and K+-ion release induced phase transition heterogeneity in tunnel MnO_2. *Adv. Funct. Mater.* **32**, 2113424 (2022).
19. Liu, L. et al. Alkali ions pre-intercalated layered MnO_2 nanosheet for zinc-ions storage. *Adv. Energy Mater.* **11**, 2101287 (2021).
20. Wu, J. et al. Bromide–acetate co-mediated high-power density rechargeable aqueous zinc–manganese dioxide batteries. *J. Mater. Chem. A.* **9**, 21888–21896 (2021).
21. Han, K. et al. High-performance aqueous Zn–MnO_2 batteries enabled by the coupling engineering of K+ pre-intercalation and oxygen defects. *J. Mater. Chem. A.* **9**, 15637–15647 (2021).
22. Wang, Z. et al. Probing the energy storage mechanism of quasi-metallic Na in hard carbon for sodium-ion batteries. *Adv. Energy Mater.* **11**, 2003854 (2021).
23. Rui, J. et al. Activation of persulfate via Mn doped Mg/Al layered double hydroxide for effective degradation of organics: Insights from chemical and structural variability of catalyst. *Chemosphere* **302**, 134849 (2022).
24. Cui, G. et al. Synthesis of nitrogen-doped KMn_8O_{16} with oxygen vacancy for stable zinc-ion batteries. *Adv. Sci.* **9**, 2106067 (2022).
25. Liu, S. et al. Structural engineering and surface modification of MOF-derived cobalt-based hybrid nanosheets for flexible solid-state supercapacitors. *Energy Storage Mater.* **32**, 167–177 (2020).
26. Sun, Z. et al. New insight on the mechanism of electrochemical cycling effects in MnO_2-based aqueous supercapacitor. *J. Power Sources* **436**, 226795 (2019).
27. Xia, H. et al. A monoclinic polymorph of sodium birnessite for ultrafast and ultrastable sodium ion storage. *Nat. Commun.* **9**, 1–10 (2018).
28. Song, X. et al. Moving MoO_2/C nanospheres with the functions of enrichment and sensing for online-high-throughput SERS detection. *Anal. Chem.* **94**, 7029–7034 (2022).
29. Chen, W. et al. Directing the deposition of lithium metal to the inner concave surface of graphitic carbon tubes to enable lithium-metal batteries. *J. Mater. Chem. A.* **9**, 16936–16942 (2021).
30. Li, X. et al. Ordered mesoporous MoO_2 as a high-performance anode material for aqueous supercapacitors. *J. Power Sources* **237**, 80–83 (2013).
31. Kang, L. et al. Dual-defect surface engineering of bimetallic sulfide nanotubes towards flexible asymmetric solid-state supercapacitors. *J. Mater. Chem. A.* **8**, 24053–24064 (2020).
32. Chang, P. et al. 3D structural strengthening urchin-like $Cu(OH)_2$-based symmetric supercapacitors with adjustable capacitance. *Adv. Funct. Mater.* **29**, 1903588 (2019).
33. Wei, X. et al. Phosphorization engineering on metal–organic frameworks for quasi-solid-state asymmetry supercapacitors. *Small* **17**, 2007062 (2021).
34. Sun, Z. et al. Photovoltaic-powered supercapacitors for driving overall water splitting: A dual-modulated 3D architecture. *Carbon Energy* https://doi.org/10.1002/cey1002.1213 (2022).
35. Liu, S. & Jun, S. C. Hierarchical manganese cobalt sulfide core–shell nanostructures for high-performance asymmetric supercapacitors. *J. Power Sources* **342**, 629–637 (2017).
36. Chen, L. et al. Interlayer engineering of K_xMnO_2 enables superior alkali metal ion storage for advanced hybrid capacitors. *ChemElectroChem* **9**, e202200059 (2022).
37. Zhang, A. et al. Adjusting the coordination environment of Mn enhances supercapacitor performance of MnO_2. *Adv. Energy Mater.* **11**, 2101412 (2021).
38. Wei, Y. et al. All pseudocapacitive MXene-MnO_2 flexible asymmetric supercapacitor. *J. Energy Storage* **45**, 103715 (2022).
39. Liu, S. et al. Phosphorus-mediated MoS_2 nanowires as a high-performance electrode material for quasi-solid-state sodium-ion intercalation supercapacitors. *Small* **15**, 1803984 (2019).
40. Zhang, A. et al. Rich bulk oxygen Vacancies-Engineered MnO_2 with enhanced charge transfer kinetics for supercapacitor. *Chem. Eng. J.* **417**, 129186 (2021).